Energy Storage Materials 17 (2019) 12–21

Contents lists available at ScienceDirect

Energy Storage Materials

journal homepage: www.elsevier.com/locate/ensm

Exceptional supercapacitor performance from optimized oxidation of graphene-oxide

Zhuangnan Li[a], Srinivas Gadipelli[a,*], Yuchen Yang[a], Guanjie He[a], Jian Guo[a], Juntao Li[a], Yue Lu[a], Christopher A. Howard[b], Dan J.L. Brett[c], Ivan P. Parkin[a], Feng Li[d], Zhengxiao Guo[a,*]

[a] Department of Chemistry, University College London, London WC1H 0AJ, UK
[b] Department of Physics & Astronomy, University College London, London WC1E 6BT, UK
[c] Department of Chemical Engineering, University College London, London WC1E 7JE, UK
[d] Shenyang National Laboratory for Materials Science, Institute of Metal Research, Chinese Academy of Sciences, Shenyang 110016, China

ARTICLE INFO

Keywords:
Carbon
Graphene-oxide
Graphene
Supercapacitor
Energy storage

ABSTRACT

Graphene-based materials are highly desirable for supercapacitors, but vary considerably in reported properties despite being prepared by similar procedures; therefore, a clear route to improve the performance is currently lacking. Here, a direct correlation between the initial oxidation of graphene-oxide precursors and final supercapacitor performance is demonstrated. Building on this significant understanding, the optimized three-dimensional graphene frameworks achieve a superior gravimetric capacitance of 330 F g^{-1} in an aqueous electrolyte. This extraordinary performance is also validated in various electrolytes at a device level. In a commercially used organic electrolyte, an excellent volumetric energy density of 51 Wh L^{-1} can be delivered, which significantly outperforms the state-of-the-art commercial carbon-based devices. Furthermore, solid-state supercapacitor with a gel electrolyte shows an impressive capacitance of 285 F g^{-1} with a rate capability of 79% at 20 A g^{-1} and capacitance retention of 93% after 20,000 cycles. This study presents a versatile design principle for engineering chemically derived graphene towards diverse applications in energy storage.

1. Introduction

Carbon networks with excellent interconnectivity, electrical conductivity and accessible porosity are showing potential for many emerging green technologies [1,2]. Templated carbon frameworks with controllable hierarchical structure over the micro- and mesoporous range promise to play a transformative role for charge storage in batteries and supercapacitors. However, the traditional methods for preparing such structures, commonly by chemical vapour deposition (CVD) and silica templating, are costly and difficult to scale, prompting extensive research into alternative viable synthesis routes [3–7]. Surface functionalized graphene (the well-known graphene-oxide, GO) and other pre-designed molecular precursor architectures, such as coordinated polymers and metal-organic frameworks (MOFs), can be used to produce a wide range of three-dimensional (3D) carbon networks [8,9]. Nevertheless, the development processes from the polymeric and MOF structures involve multi-task control over thermolysis at elevated temperatures and/or inherent metal etching [10–12]. In contrast, the formation of 3D graphenic networks from hydrophilic GO sheets is relatively straightforward and scalable *via* a hydrothermal route at comparatively low temperatures [13,14].

Most hydrothermally reduced GO (htrGO) structures are developed from a GO precursor, which is usually derived by direct oxidation of graphite in a top-down approach using Hummers' or a related method [15–23]. The oxidation process leads to the extensive introduction of hydrophilic functional groups onto the graphene sheets, in the form of epoxides, hydroxyls and carboxyls. These groups can form hydrogen-bonds with water molecules, which intercalate between the graphene sheets weakening interlayer van der Waals attractions and facilitating aqueous dispersion [14,15]. The resulting dispersions, which contain predominantly single or few layered GO nanosheets, can be used to develop 3D networks under hydrothermal conditions, where the reduced GO as the main building blocks [8]. During the hydrothermal treatment, the reduced GO sheets tend to physically cross-link each other, due to the gradually restored π–π interactions [13]. Surface oxygen-containing functional groups are mainly reduced by dissociation in the form of CO_2 [17]. This process produces carbon vacancies on the graphene basal plane, which can generate defective sites and nanopores. In addition, the entrapment of CO_2 bubbles creates void

* Corresponding authors.
E-mail addresses: s.gadipelli@ucl.ac.uk (S. Gadipelli), z.x.guo@ucl.ac.uk (Z. Guo).

https://doi.org/10.1016/j.ensm.2018.12.006
Received 15 September 2018; Received in revised form 3 December 2018; Accepted 4 December 2018
Available online 06 December 2018

spaces within the networked structure. Together, the resultant 3D htrGO frameworks with hierarchical pores and substantial surface area are promising for efficient charge storage and transport.

Thus far, several porous htrGO frameworks have been developed and their performance investigated as supercapacitor electrodes [13,18–23]. Nevertheless, despite being processed under similar hydrothermal conditions, such structures show distinctly different charge storage capacities, ranging from 110 to 240 F g^{-1} at 1 A g^{-1} in an aqueous electrolyte. For example, the pioneering work by Shi et al. exhibited a specific capacitance of 160 F g^{-1} (where the GO was prepared by a modified Hummers' method) [13]. Subsequently, Yang et al. reported a capacitance of 235 F g^{-1} with the same GO synthesis route [19]. In another case, the htrGO structures prepared from GO by the traditional Hummers' method yielded a specific capacitance of 116 F g^{-1} [20]. Xu and co-workers reported a comparably high capacitance of > 300 F g^{-1}, through etching of htrGO with H_2O_2 [18]. Such discrepancies have not been clearly addressed before and indicate poor understanding of precursor-directed structural development. Thus, it is of great significance to clarify the achievable structure-performance relationships in order to further improve energy storage capacities.

In this work, this discrepancy is investigated by performing a systematic study of the htrGO frameworks engineered to have different level of initial oxidation (Fig. 1). The initial oxidation is demonstrated to have a profound effect on the energy storage behaviour of the resultant materials, by means of determining their surface and interface properties. These key features include development of open framework structures with pore sizes across different length scales, accessibility and conduction/transportation for ionic charges, and density of oxygen-containing functional groups on the surface. The understanding gained can lead to a significantly improved capacitance. For instance, the structure produced from optimized GO achieves a specific capacitance of 330 F g^{-1} at 1 A g^{-1} in an aqueous electrolyte, which is one of the highest among all dopant-free graphene-based materials reported to date. More importantly, the exceptional performance is also validated under a diverse range of working conditions with different electrolytes, including acidic (H_2SO_4), basic (KOH), organic (tetraethylammonium tetrafluoroborate, $TEABF_4$) and gel (polyvinyl alcohol (PVA)/H_2SO_4), at the device level. The as-fabricated flexible supercapacitor with the gel electrolyte exhibits an excellent specific capacitance (285 F g^{-1} at 1 A g^{-1}), rate capability (~79% at 20 A g^{-1}) and cyclic stability (~93% retention after 20,000 cycles). Furthermore, a device with the organic electrolyte can readily deliver a considerably high volumetric energy density of 51 Wh L^{-1}. This significantly outperforms commercial carbon-based supercapacitors and is comparable to the state-of-the-art batteries [24].

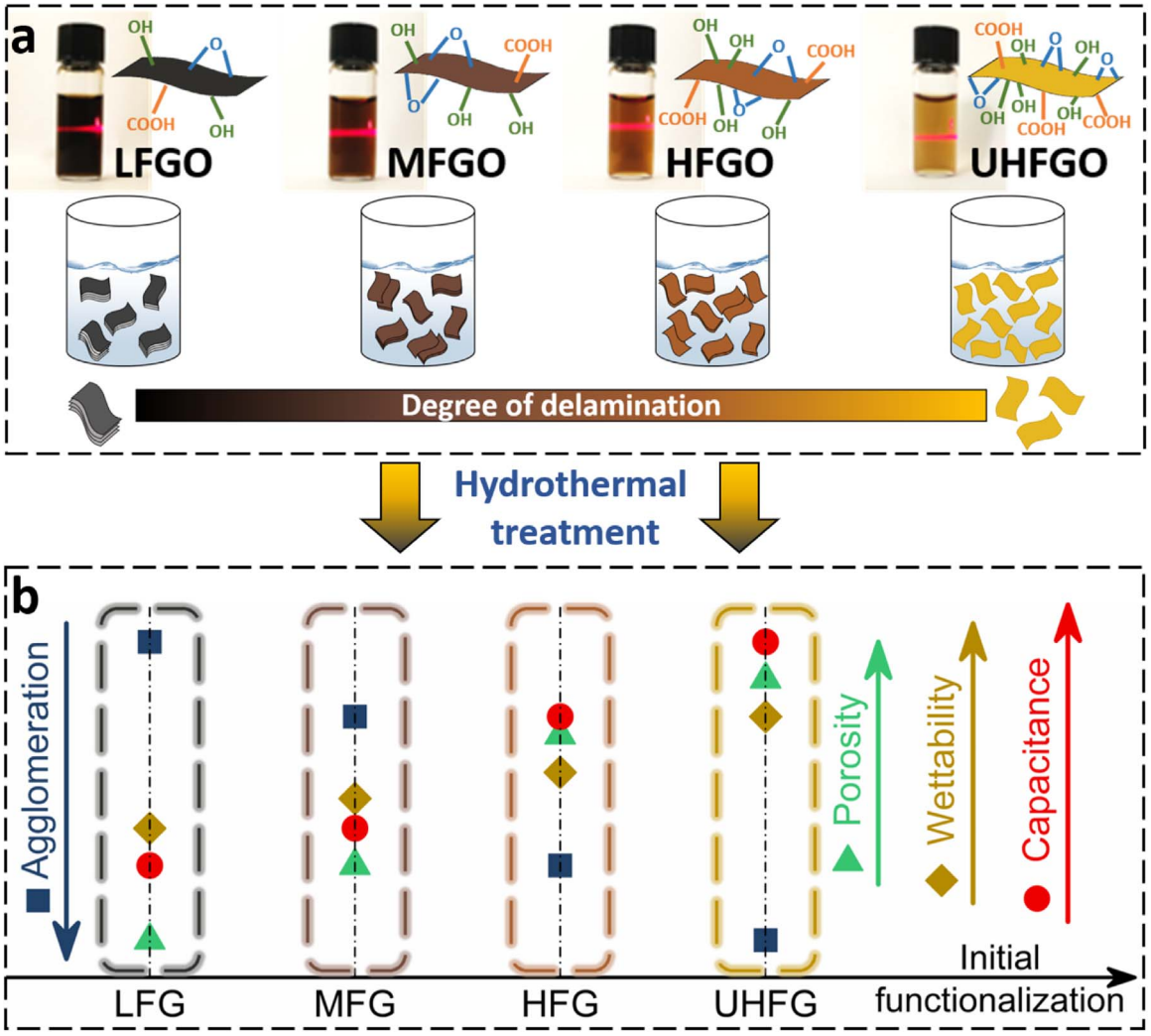

Fig. 1. Schematic diagram illustrating the production of 3D htrGO frameworks with controllable functionalization. (a) Photographs of aqueous dispersions (2 mg ml^{-1}) of each GO precursor (top), showing the Tyndall effect. The corresponding structural illustration indicates the degree of delamination increasing with the functionalization (bottom). (b) Graphical summary for the formed 3D htrGO frameworks of their relative structure and performance versus the increasing level of initial functionalization.

2. Results and discussion

2.1. Preparation and structural characterizations

A series of GO precursors with different concentrations of oxygenated functionalities were first synthesized from natural graphite powder *via* the Hummers' method and further modification (see Experimental section). By controlling the oxidation, the as-prepared GO precursors exhibit tuneable oxygen contents of 27.1, 29.5, 31.1 and 33.9 at% (Fig. S1), respectively named as low-level oxygen-functionalized GO (LFGO), medium-level oxygen-functionalized GO (MFGO), high-level oxygen-functionalized GO (HFGO) and ultrahigh-level oxygen-functionalized GO (UHFGO). These GO samples were then dispersed in water by ultrasonication, as evidenced by the strong Tyndall scattering effect for an incident laser beam (Fig. 1**a**). Notably, a higher concentration of functionalities on the GO sheets results in better dispersion, owing to the increased number of functional group-water interactions. This is further confirmed with the enhancement in transparency of the GO dispersions, from LFGO to UHFGO, in accordance with the decreased π–conjugated sp^2 carbon domains. Moreover, the relatively small conjugation area with an increased level of oxidation of GO leads to weaker π–π interactions, and thus readily produces entirely delaminated single sheets (atomic force microscopy (AFM) images in Fig. S2) [25]. Such delamination has a profound influence on the structural development of the desirable 3D htrGO frameworks (as discussed later). Each aqueous dispersion of GO was then individually sealed in a Teflon-lined autoclave and subjected to hydrothermal treatment. During this process, the GO sheets are reduced and simultaneously self-assemble into an interconnected 3D architecture (denoted as LFG, MFG, HFG and UHFG in accordance with the corresponding GO precursor). It is worth noting that the derived products exhibit very different layered assemblies and networked structures (Fig. 2**a-d** and S3). Extensive cross-linking of spongy graphene layers is found in HFG and UHFG; whereas, LFG contains densely clumped layers. Transmission electron microscopy (TEM) images also reveal the delaminated but interconnected layers in UHFG (Fig. S4). The spongy or wrinkled nature of the graphene sheets correlates with the increasing density of surface functionalities, which induces morphological effects on the pristine carbon lattice.

X-ray photoelectron spectroscopy (XPS) survey spectra show an oxygen content of 11.2, 13.4, 14.7 and 16.0 at% for LFG, MFG, HFG and UHFG, respectively (Fig. S5 and Table S1). Detailed analysis of C 1 s spectra indicates that these residual oxygen-containing functional groups exist mainly as epoxides (C–O) and carboxyls (C═O) (Fig. 3**a** and Table S2). In addition, the relatively larger residual oxygen content is also supported by the weight loss behaviour observed in thermogravimetric analysis (TGA) (Fig. S5). The two-step mass loss in the region of < 150 °C and 200–300 °C reveals the nature of oxygen in the form of bound water within wrinkled graphene networks and actual surface bonded C–O/C═O, respectively [26]. It is worth noting that the sp^3-bonded carbon species and dissociated carbons in the lattice induce significant disorder on the basal plane [27,28]. This disorder is demonstrated by an increase in the intensity ratio of the D to G band in the Raman spectra (Fig. 3**b** and S6). The excess defects and residual functionalities can enhance the hydrophilicity of the carbon frameworks. For example, the UHFG displays a much lower static water contact angle than other less functionalized samples (Fig. 3**c**). The nitrogen adsorption/desorption isotherms of the samples exhibit a typical H3 loop, indicating the coexistence of micro-, meso- and macropores (Fig. 3**d**) [29]. Further analysis shows that the specific surface areas are 68, 102, 456 and 512 m^2 g^{-1}, respectively for LFG, MFG, HFG and UHFG. The total pore volume and pore size distribution in the samples are also increased from LFG to UHFG (Fig. 3**e**).

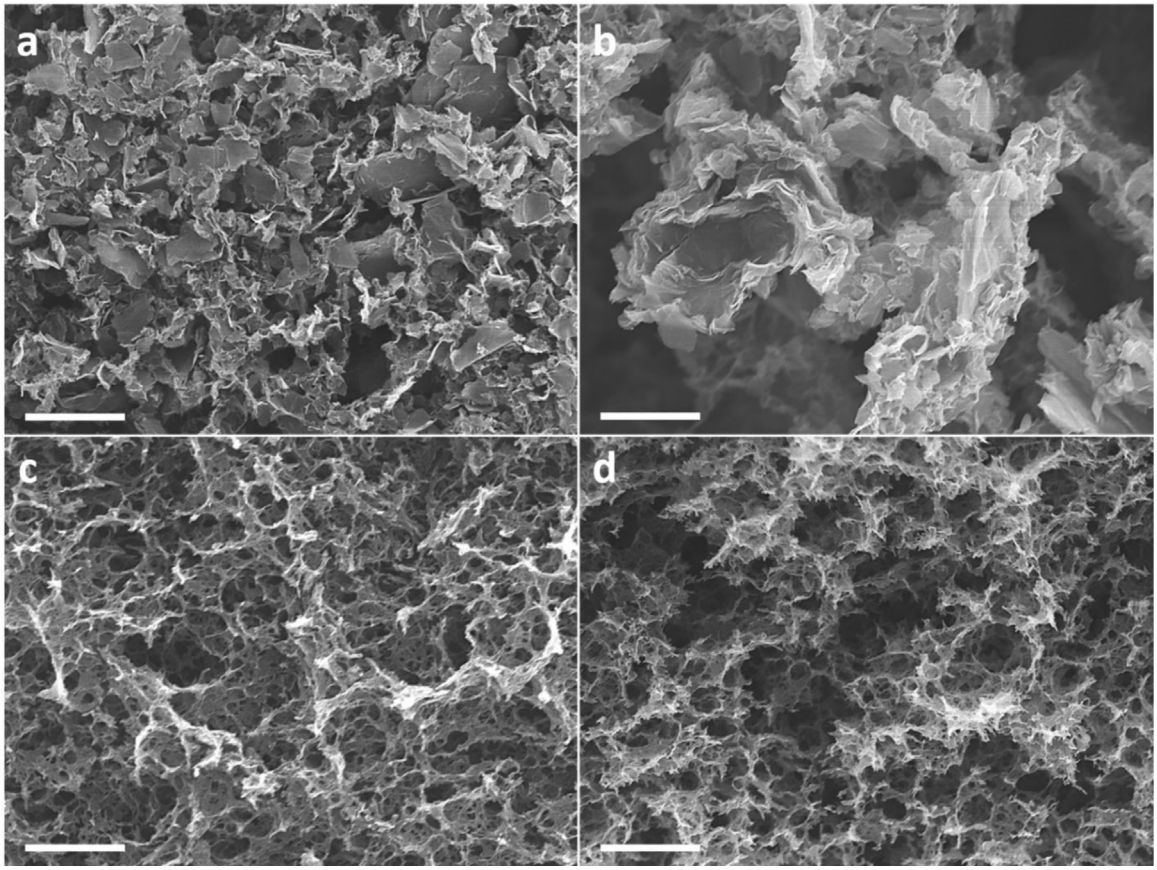

Fig. 2. Morphology of 3D htrGO frameworks. (a-d) SEM images of LFG (a), MFG (b), HFG (c) and UHFG (d). Scale bars, 5 μm.

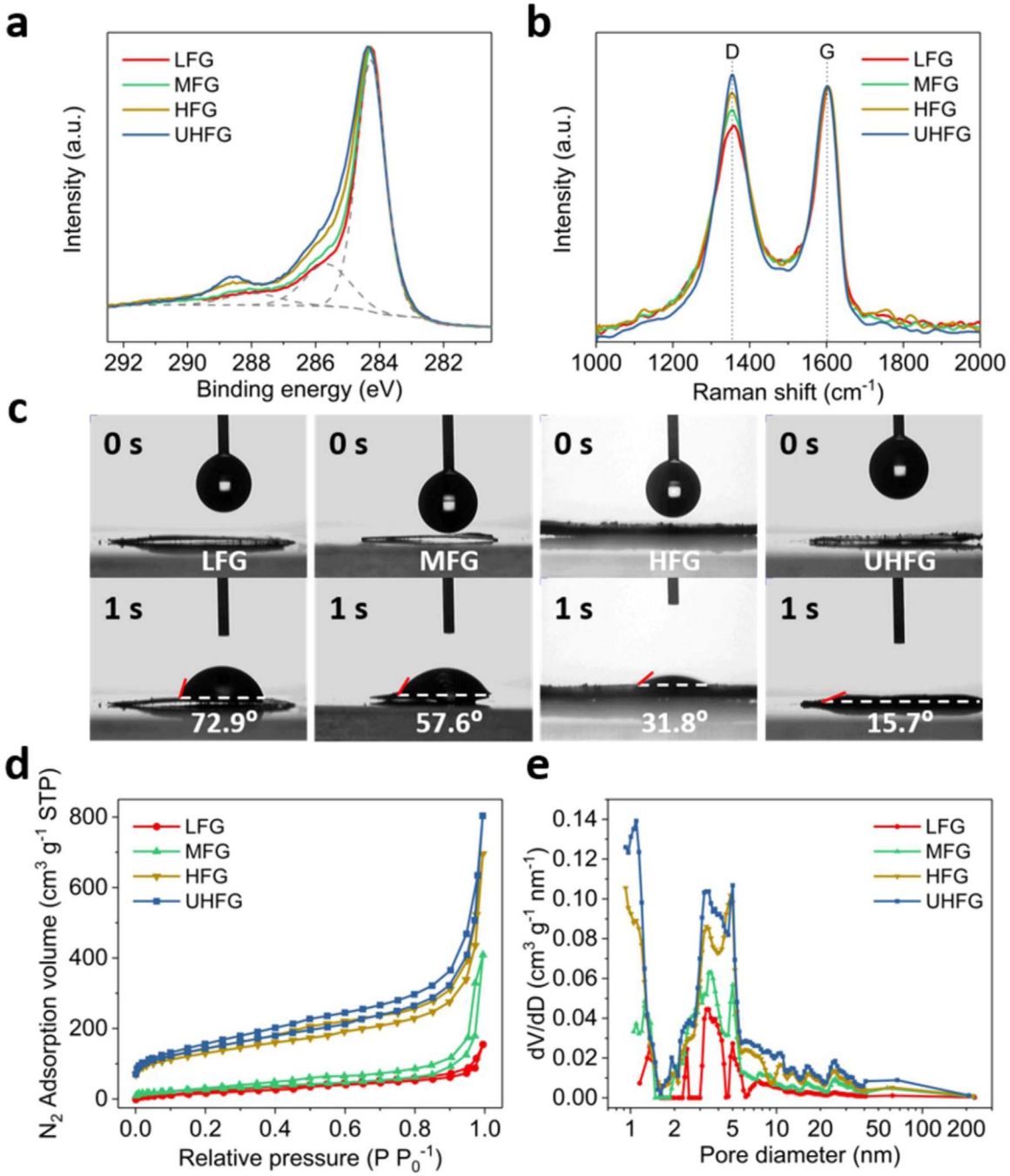

Fig. 3. Structural characterization of LFG, MFG, HFG and UHFG. (a) XPS C 1 s spectra. The fitting components with peak at ~284.6 eV represent the sp^2 carbons, the component at ~286.0 eV is due to residual C–O bonds and possible the sp^3 bonding carbons, and the peak at ~287.9 eV is related to the remaining C=O bonds. (b) Raman spectra. The I_D/I_G ratio represents the density of defects and disorder in the carbon structures. An increased ratio is seen in the order of LFG (0.85), MFG (0.91), HFG (0.98) and UHFG (1.04). (c) Water contact angle measurements showing a progressive hydrophilicity of LFG < MFG < HFG < UHFG. (d, e) N_2 adsorption-desorption isotherms (d) at 77 K and their corresponding pore size distribution (e).

2.2. Electrochemical characterizations

The capacitive performance of the materials was first evaluated in a three-electrode configuration with 1.0 M KOH aqueous electrolyte. Each sample exhibits a quasi-rectangular cyclic voltammetry (CV) curve and an almost isosceles triangular-shaped galvanostatic charge-discharge (GCD) curve, respectively (Fig. 4**a, b**). Both characteristics indicate a nearly ideal capacitive behaviour. Since the specific capacitance is proportional to the geometric area of the CV curves at a given scan rate, the specific capacitance increases in the order of LFG, MFG, HFG and UHFG (Fig. 4**a**). Accordingly, the GCD curves exhibit comparably longer discharge time (Fig. 4**b**). The gravimetric capacitances of the electrodes derived at different current densities are summarized in Fig. 4**c**. UHFG delivers a remarkable specific capacitance of 330 F g^{-1} at 1 A g^{-1}; whereas, the others show 278 (HFG), 214 (MFG) and 181 F g^{-1} (LFG). Such a specific capacitance (330 F g^{-1}) is one of the highest ever reported for dopant-free graphene-based structures (Fig. S7 and Table S3). At a relatively high current density of 50 A g^{-1}, the UHFG can still retain ~78% of its initial value (256 F g^{-1}). In contrast, the capacitance retention is only 66–55% for HFG to LFG. Such a distinction of rate capabilities is ascribed to the different charge-storage mechanisms and ion transport properties of the elec-

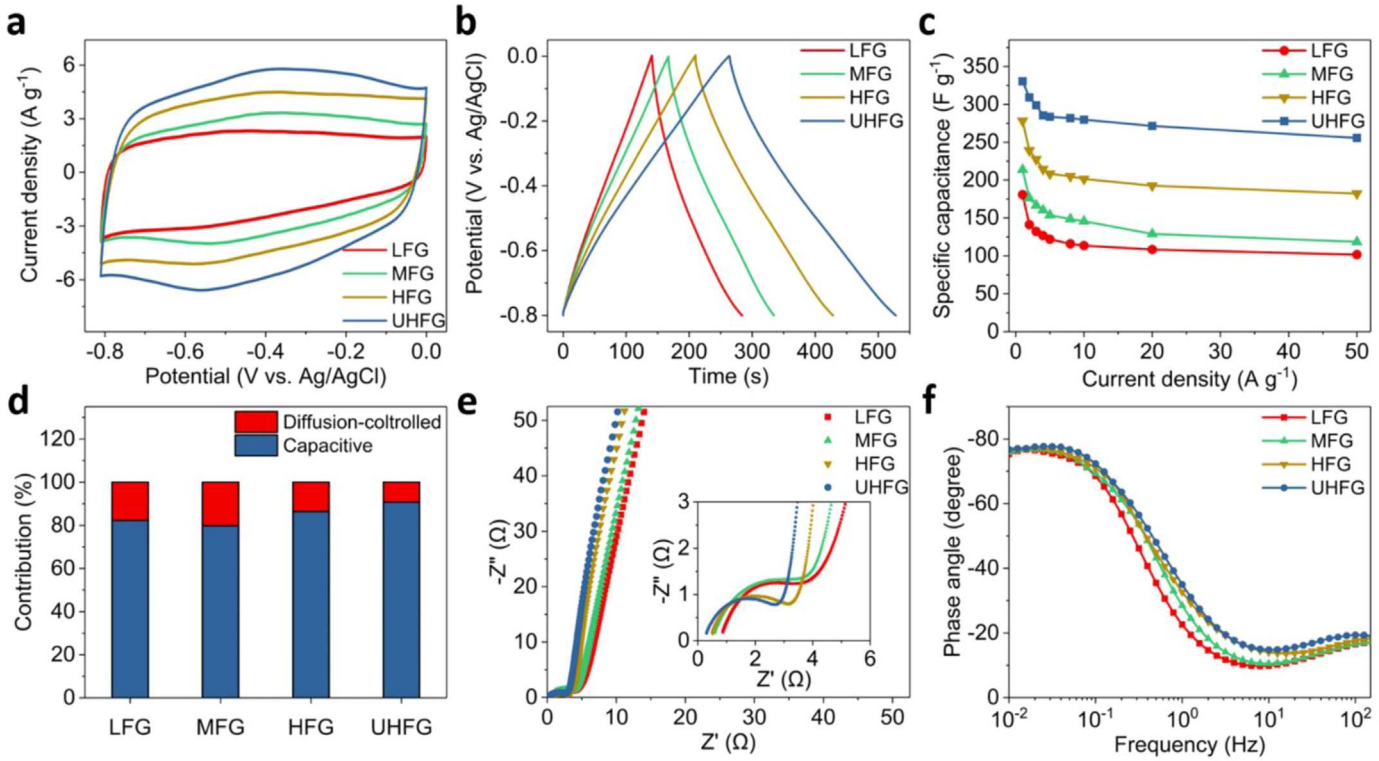

Fig. 4. Electrochemical characterization of LFG, MFG, HFG and UHFG in 1.0 $_{M}$ KOH with a three-electrode configuration. (a) CV curves at the scan rate of 20 mV s^{-1}. (b) GCD curves at the current density of 1 A g^{-1}. (c) Comparison of specific capacitances versus current densities. (d) Capacitance contribution differentiation at the scan rate of 5 mV s^{-1}. (e) Nyquist plots. The inset shows the magnified high-frequency region. (f) Bode plots of impedance phase angle versus frequency.

trode materials, as specified below with the assistance of capacitance differentiation and electrochemical impedance spectroscopy (EIS), respectively.

The current responses in the CV curves can be separated into capacitive and diffusion-controlled contributions, associated to the surface (*i.e.* electrical double-layer (EDL) capacitance and near-surface redox reactions) and intercalation (*i.e.* fast ion insertion/extrusion in bulk materials) processes, respectively (Fig. S8) [30]. Samples reveal a dominant capacitive charge-storage mechanism, with ~91%, 87%, 80% and 82% capacitive contribution to the total capacitance in the UHFG, HFG, MFG and LFG, respectively (Fig. 4**d**). Therefore, UHFG can exhibit the best rate capability, owing to the fact that the surface capacitive behaviour is comparably more stable at a higher scan rate/current density than the diffusion-controlled processes [30]. Nyquist plots for all samples show a nearly vertical slope in the low-frequency region, suggesting an ideal capacitive behaviour (Fig. 4**e**). However, clear differences among the curves are observed in the magnified high-frequency region (Fig. 4**e**, inset). A smaller diameter of the semicircle and a shorter 45° Warburg region indicate a lower charge transfer resistance and more efficient electrolyte accessibility within the structures (Fig. S9) [31]. Therefore, UHFG exhibits the best ionic mobility and electrolyte transport capability. The characteristic performance of UHFG is also evidenced in the Bode plots with rapid frequency response (Fig. 4**f**). At the phase angle of –45°, where the capacitive and resistive impedances are equal [31], UHFG reflects a characteristic frequency (f_0) of 0.71 Hz, which corresponds to a relaxation time constant τ_0 (= $1/f_0$) of 1.4 s, much smaller than those of HFG (2.0 s), MFG (2.2 s) and LFG (3.0 s) as well as the commercial activated carbons (~10 s) [32].

The UHFG reveals an outstanding energy storage capacity amongst peer htrGO samples and other reported graphene-based structures (Table S3) [13,18–23]. This advancement and the related performance of the studied samples correlate well with the degree of initial oxidation of the GO precursors (Fig. 1**b**). Here, it should be pointed out that merely a high level of oxidation for GO is insufficient to ensure the capacitance promotion, due to the concomitant induced damage of the aromatic lattice. For instance, the htrGO prepared from an overly oxidized GO precursor shows a decreased capacitance, which is further evidenced by the more resistive ionic transport behaviour and unfavourable structural characteristics (Fig. S10). Therefore, the precise control over the degree of oxidation of GO is a prerequisite for the improved capacitive performance with referring to the characteristic structural development (Fig. S11). It is worth mentioning that the samples (LFG, MFG and HFG) with the specific capacitance (160 to 280 F g^{-1}) and the initial level of precursor oxidation (C/O ratio from 2.7 to 2.2) closely resemble the structures reported in previous studies [13,18,19,21,23]. An increased oxygen content of about 7 at% from LFGO (C/O ratio of 2.7) to UHFGO (C/O ratio of 1.9) leads to prominent structural benefits in the produced htrGO frameworks. Enhanced porosity of UHFG across the micro- and meso- pore region facilitates the efficient charge storage and transfer (Fig. S12). More precisely, the high total pore volume and the hierarchical porous structure guarantee abundant spaces for the electrolyte ion distribution and charge separation within the networks. Ions in the electrolyte can penetrate/diffuse into the small pores, thus high micropore volume can effectively contribute to charge storage and enhance the total capacity. On the other hand, the hierarchical pores in the micro- and meso-porous region provide unobstructed channels for rapid ion transport [6,19].

Furthermore, the abundant residual oxygen-containing groups of UHFG favourably introduce additional pseudocapacitance by means of redox reactions, including > C–OH ↔ C=O + H^+ + e^-, –COOH ↔ –COO + H^+ + e^- and > C=O + e^- ↔ > C–O^- [26]. The calculation according to the Trasatti method indicates ~40% overall capacitance is contributed by pseudocapacitance (Fig. S13) [33]. This is also well supported by the EDL capacitance obtained from the same sample after high-temperature heat treatment. About 40% drop of the overall capacitance is measured due to the removal of the oxygenated

functional groups (Fig. S13). Moreover, the presence of such surface functionalities results in the improved hydrophilicity of UHFG. The wettability of the active electrode material in the electrolyte is another crucial factor to enhance the supercapacitor performance, where a more effective contact at the solid-liquid interface leads to efficient capillary action of the pores and thus produces further ion accessible surface area. Therefore, the specific capacitance can be significantly enhanced by incorporating oxygenated surface functionalities within the graphene structures.

It is worth noting that, referring to the structures with similar specific surface areas that show ~150 F g^{-1} [34–37], the EDL capacitance of UHFG is still at least 30% higher. This can be attributed to the effect of sheet morphology. For example, the structures with relatively flat and fragmented graphene sheets developed by thermal-shock or chemical reduction usually show weak interconnectivity, which are less efficient for charge transfer [34,35,37]. In contrast, the highly interconnected crumpled sheets in the UHFG can entrap water within the networks and those wrinkles also act as fluid channels for electrolytes, both of which are comparably favourable for charge migration and accessibility. In addition, unlike flat sheets that pack tightly during the electrode preparation and thus significantly sacrifice the accessible surface area, the wrinkled sheets can preserve majority of surface area after processing of the electrode [38,39]. Another important factor is the number of layers, which is essentially determined by the concentration of GO dispersions during preparation. In this study, 2 mg ml^{-1} was proven to be the optimized concentration to achieve a good balance between network forming and layer assembly (Fig. S14). Together, the preceding structural features in synergy contribute to the overall energy storage performance of the system, which enable the representative 3D graphene frameworks to show a positive correlation with the initial level of oxidation in the GO precursors (Fig. S15).

2.3. Supercapacitor performance

The UHFG, with its outstanding electrochemical properties, was further explored at the device level by the fabrication of symmetric supercapacitors under both acidic (1.0 M H_2SO_4) and basic (6.0 M KOH) working conditions. A similar capacitive behaviour of the UHFG is observed in both aqueous electrolytes (Fig. 5 and S16). It is also worth mentioning that the supercapacitors constructed with all four samples revealed the similar characteristic trend as those measured in the three-electrode configuration (Fig. 4 and S16). Since energy stored in the device is proportional to the square of the operating voltage, considering the limitation of aqueous electrolytes (usually < 1.0 V to prevent water electrolysis, with a theoretical limit of 1.23 V), the supercapacitors were also constructed with a commercial organic electrolyte (1.0 M $TEABF_4$ in acetonitrile) to extend the voltage window. In both cases, the CV curves show a rectangular-like shape (Fig. 5**a, b**), suggesting a nearly ideal capacitive behaviour of the UHFG, which is further confirmed by the quasi-triangular nature of the GCD curves (Fig. 5**c, d**). Fig. 5**e** presents the specific capacitances of the sample at different current densities, in each device. At 1 A g^{-1}, the UHFG exhibits a specific capacitance of 286 and 182 F g^{-1} for aqueous and organic working conditions, respectively. With an increasing current density to 20 A g^{-1}, the electrode retains ~85% (244 F g^{-1}) in H_2SO_4, whereas it is ~75% (136 F g^{-1}) in $TEABF_4$. Such a difference is also reflected by a minor voltage drop and comparatively less fusiform-like shape of the GCD and CV curves, respectively, in H_2SO_4 (Fig. 5**a-d**). This is because the unfavourable influence of the lower conductivity, higher viscosity and larger solvated ion size of $TEABF_4$ [5,7,40]. More specifically, the bare/solvated sizes of both TEA^+ (0.67/1.30 nm) and BF_4^- (0.45/1.16 nm) ions are relatively large than the H^+ (0.12/0.28 nm) ions in aqueous electrolytes (Fig. S17). This result is consistent with the previously reported studies, which indicate that a comparably larger size of the pores is desired for adapting to the organic electrolytes [41,42].

The gravimetric energy density of UHFG delivered in the aqueous electrolytes is about 6.5 Wh kg^{-1}, comparable to or higher than other reported values [1,8,28]. Due to the extended operating voltage in the organic electrolyte, the sample yields a superior energy density of 46 Wh kg^{-1}, which is over seven times higher than it in the aqueous condition (Fig. S18). Furthermore, both devices show considerably high cyclic stability, with a capacitance retention of ~98% and ~87% after 20,000 cycles at 10 A g^{-1} in H_2SO_4 and $TEABF_4$ electrolyte, respectively (Fig. 5**f**). The more capacitance degradation in the $TEABF_4$ electrolyte can be ascribed to the comparably low mobility of organic ions, which results in irreversible charge accumulation during the long term cyclic tests [40].

2.4. Comparison of energy storage features

With the development of portable power supplies, high volumetric energy storage capacity becomes a determinant factor. To this end, the volume of the entire device including two active electrodes, two current collectors and separator should be considered (Fig. S19) [43]. Therefore, a larger amount of active materials is required to increase its volume fraction in the device and thereby maximize the stack energy density (see details in Methods). However, this is not straightforward since the increase of material loading usually comes at the compromise of the capacitive performance [24]. It is worth noting that the UHFG as a working electrode with an areal mass loading of up to 10 mg cm^{-2} (comparable to commercial carbon-based supercapacitors) [24] exhibited almost the same charge/discharge behaviour as the one with lower loading (1 mg cm^{-2}) (Fig. S20 and S21). The electrode shows a high gravimetric and volumetric specific capacitance of 170 F g^{-1} and 189 F cm^{-3}, respectively at 1 A g^{-1} (Fig. 6**a**). This leads to an excellent volumetric energy density of 51 Wh L^{-1}, outperforming many reported carbon-based electrodes (Fig. S22 and Table S4). Consequently, the entire device delivered a stack volumetric energy density of 36.5 Wh L^{-1} within a 2.7 V operating voltage. The high power density is the most significant characteristic of the supercapacitors; therefore, the energy density delivered under relatively high power density conditions is a key parameter to evaluate the true performance of practical supercapacitors. Remarkably, the device still maintains the energy density of 24.7 Wh L^{-1} at a high stack volumetric power density of > 10,000 W L^{-1}. Further comparison of energy storage features with the state-of-the-art technologies is illustrated in the Ragone plots (Fig. 6**b**). Clearly, the UHFG-based device significantly outperforms commercial supercapacitors and is superior to those of previous studies (Table S4) [7,18,32,44–48]. Such performance is even comparable to the lead-acid batteries in terms of energy density [18], demonstrating great potential for a broad range of practical applications.

2.5. Fabrication of all-solid-state supercapacitor (ASSC)

With the rising demand of wearable and flexible electronics, an ASSC was fabricated by utilizing UHFG electrodes. The construction of this device is illustrated in Fig. 7**a**. Two UHFG coated flexible carbon cloth substrates were assembled symmetrically with the PVA/H_2SO_4 gel in between, which acts as both the electrolyte and separator. Such a device shows a negligible change of its overall capacitive behaviour when subjected to arbitrary twisting or bending (Fig. 7**b**). The device also exhibits excellent electrochemical performance, even comparable to the aqueous system. For example, the specific capacitance of 285 and 226 F g^{-1} at 1 and 20 A g^{-1}, respectively, closely match the values of 286 and 244 F g^{-1} observed in 1.0 M H_2SO_4 aqueous electrolyte (Fig. 7**c**). Such prominent specific capacitance and rate capability (~79% at 20 A g^{-1}) are at the top-level among reported ASSC devices (Table S5), and is attributed to an effective infiltration of the gel electrolyte into the UHFG frameworks [49,50].

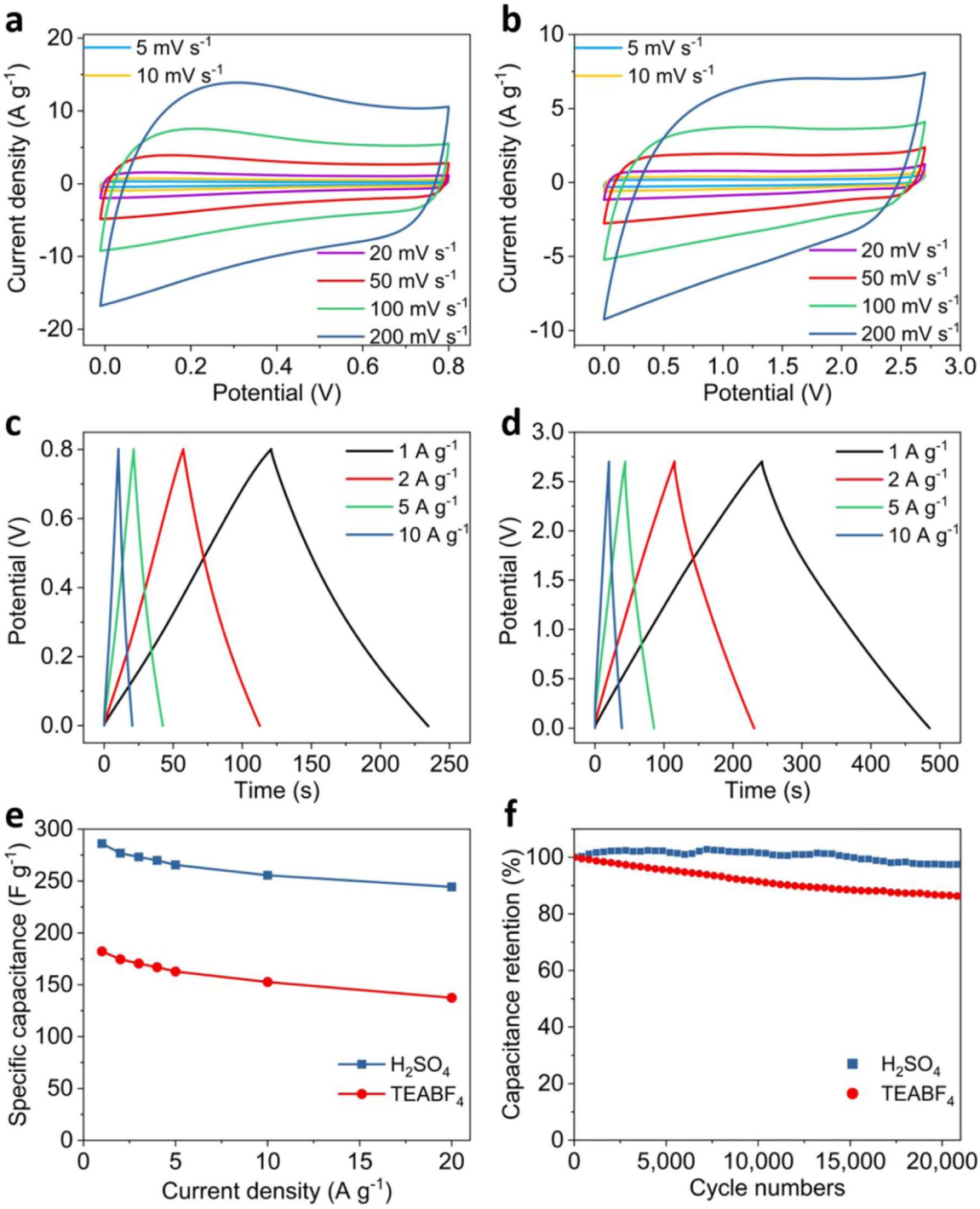

Fig. 5. Symmetric supercapacitor performance of UHFG in various electrolytes. (a, b) CV curves at different scan rates in 1.0 M H_2SO_4 (a) and 1.0 M $TEABF_4$ (b), respectively. (c, d) GCD curves at different current densities in 1.0 M H_2SO_4 (c) and 1.0 M $TEABF_4$ (d), respectively. (e) Specific capacitances versus current densities. (f) Cyclic stabilities for GCD cycles at the current density of 10 A g^{-1}.

To widen the operating voltages, tandem devices were fabricated by directly connecting several ASSC units in series. The voltage window is extended to 1.6 and 2.4 V with two and three units, respectively (Fig. 7**d**). More importantly, a nearly unchanged charge/discharge profile for the tandem device compared with the single one, suggests the well-maintained capacitive performance of each individual unit (Fig. 7**e**). A light-emitting diode (LED) powered by the tandem device further reveals its potential for practical applications (Fig. 7**f**, inset). Moreover, the device demonstrates an outstanding durability with a capacitance decay of only ~7% after 20,000 GCD cycles at 10 A g^{-1} (Fig. 7**f** and S23).

3. Conclusions

In summary, a series of GO-based materials were systemically developed to investigate the significance of the initial oxidation level for their capacitive energy storage. It is found that several structural features of the final product (htrGO frameworks), such as extent of the sheet delamination, formation of networking interconnectivity, residual surface oxygen functional groups, wettability and the accessible porosity for ionic charges, can be directly managed by control over the degree of the initial oxidation of the GO precursor. Based on this in-depth understanding of the system, the optimized UHFG structure

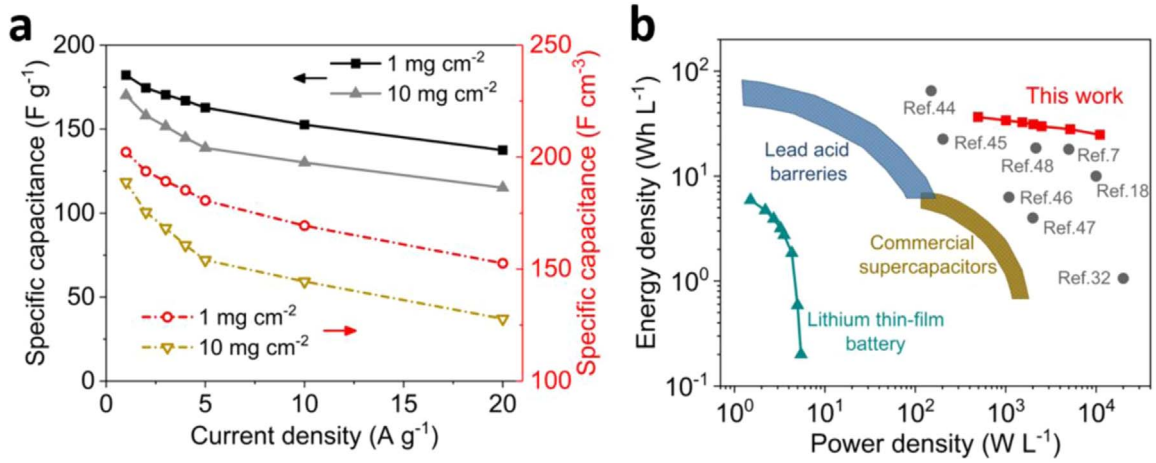

Fig. 6. Volumetric energy storage features of the UHFG-based supercapacitor with increased areal mass loading. (a) Comparison of gravimetric and volumetric capacitances versus current densities, respectively. (b) Volumetric Ragone plots of the UHFG-based supercapacitor (with 10 mg cm^{-2} mass loading per electrode) in comparison with reported values and the state-of-the-art energy storage devices (including commercial supercapacitors, lead-acid batteries and lithium thin-film battery) [24]. Note that all energy density and power density values here are calculated based on the entire device, containing two working electrodes, two current collectors and separator.

exhibits one of the highest gravimetric specific capacitance values reported to date for peer materials in the aqueous electrolyte. Such impressive capacity is well maintained in various commonly used electrolytes in the practicable supercapacitor devices. For instance, the all-solid-state supercapacitor in a gel electrolyte demonstrates top-level performance amongst practical carbon-based flexible devices, in particular the specific capacitance, rate capability and cyclic stability. More remarkably, the fabricated supercapacitor in an organic electrolyte delivers an exceptional stack volumetric energy density under a high power density condition, which represents a promising candidate to bridge the gap between traditional capacitors and batteries. This study could lead to further advancements in the design principles used to engineer chemically derived graphene, and broaden the opportunities for a wide range of energy related applications.

4. Experimental section

4.1. Formation of 3D htrGO frameworks with controllable functionalization

GO precursors were synthesized by a modified/improved Hummers' method [16,50,51]. To prepare UHFGO, graphite powders (1 g) were added to 9:1 mixture of concentrated H_2SO_4 and H_3PO_4 (22.5 ml: 2.5 ml) under vigorous stirring at 0 °C. Next, $KMnO_4$ (6 g)

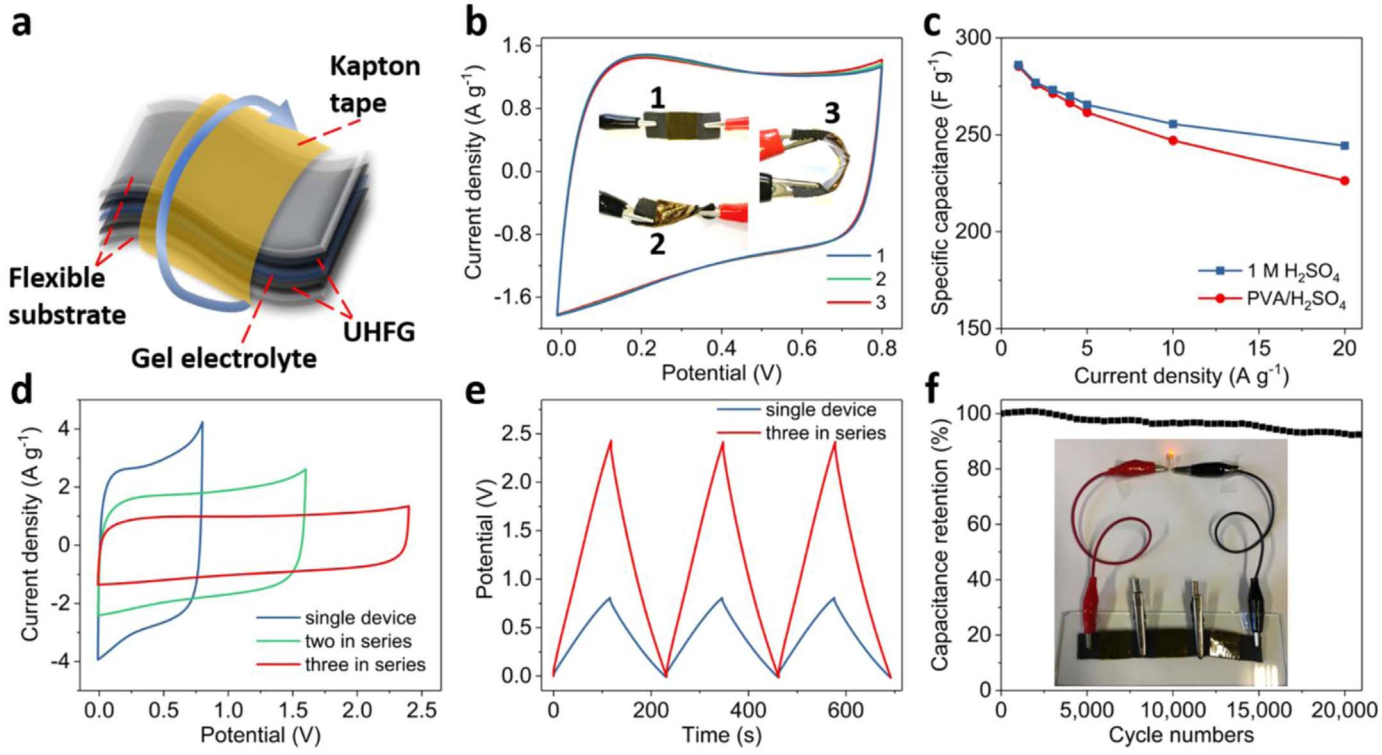

Fig. 7. Flexible ASSC based on UHFG electrodes in PVA/H_2SO_4 gel electrolyte. (a) Schematic illustration of the device configuration. (b) CV curves of the device under different deformation conditions at the scan rate of 20 mV s^{-1}. (c) Comparison of specific capacitances versus current densities. (d) CV curves of single and two/three in-series devices at the scan rate of 50 mV s^{-1}. (e) GCD curves of single and three in-series devices at the current density of 1 A g^{-1}. (f) Cyclic stability of the device for 20,000 GCD cycles at a current density of 10 A g^{-1}. The inset shows an LED powered by the tandem device.

was slowly added to the mixture under persistent stirring at a temperature below 5 °C. The mixture was further cooled to 0 °C and stirring was maintained overnight. The mixture was then slowly heated to 50 °C in an oil bath and left for a day resulting in a brown paste. Deionized (DI) water (120 ml) was added slowly to the paste and stirred for 1 h. Subsequently, H_2O_2 (35%, 9 ml) was added to the solution drop by drop to reduce the unreacted excess $KMnO_4$, during this process the colour of the solution changed to bright yellow. The solution was stirred for another 1 h and left to settle. Then the product was washed using diluted HCl (3.5%, 750 ml) to remove remaining salts, followed by washing with DI water until neutral. Finally, the UHFGO powder was obtained by freeze-drying. LFGO, MFGO and HFGO were synthesized by similar procedures but with 2, 3 and 4 g $KMnO_4$, respectively. Note that no H_3PO_4 was added for the MFGO synthesis.

The reduction of GO was carried out by a hydrothermal treatment. Firstly, a homogeneous GO dispersion (2 mg ml^{-1}) was prepared by ultrasonication of the GO powder in DI water, followed by centrifugation (2000 rpm for 10 min). Subsequently, 25 ml of the GO aqueous dispersion was sealed in a 50 ml Teflon-lined autoclave and maintained at 180 °C for 12 h. After being freeze-dried, the obtained htrGO frameworks were named as LFG, MFG, HFG and UHFG in corresponding to GO precursors.

4.2. Structural characterization and analysis

The morphologies were investigated with scanning electron microscopy (SEM, Jeol 6700), TEM (Jeol 2100) and AFM (Keysight 5600LS). TGA was carried out on Setsys (Setaram Instrument) at a heating rate of 3 °C per min under a N_2 atmosphere. XPS measurements were investigated with an Al-Kα source (Thermo Scientific). Raman spectra were recorded with a 514.5 nm laser beam (Renishaw). The N_2 adsorption-desorption isotherms were measured at 77 K (Quantachrome Autosorb-iQC). The specific surface area was calculated from isotherms based on the Brunauer-Emmett-Teller (BET) method. The pore size distribution was obtained from desorption data according to a combination of quenched solid density functional theory (QSDFT) for micro- and meso- pores < 50 nm and the Barrett-Joyner-Halenda (BJH) method for macropores > 50 nm [52]. The water contact angles were measured *via* the sessile-drop method at ambient temperature using an optical contact angle meter (FTA 1000, water droplet is 5 μL).

4.3. Fabrication of supercapacitors

The working electrode was prepared by fully mixing 90 wt.% active material and 10 wt.% PTFE (60 wt.% dispersion in water) into a paste using an agate mortar and pestle, followed by compressing the mixture onto the current collector (nickel foam) at 25 MPa for 1 min and then drying at 120 °C for 6 h. The symmetric supercapacitor was fabricated by assembly of two working electrodes and a cellulose-based membrane separator into a sandwich-like structure in CR2032 stainless-steel coin-cell cases along with the electrolyte (6.0 M KOH) at ambient conditions. For acidic (1.0 M H_2SO_4 and PVA/H_2SO_4) and organic (1.0 M $TEABF_4$ in acetonitrile) electrolytes, carbon paper and aluminium foils were used as the current collectors, respectively. In the case of supercapacitors with the organic electrolyte, 10 wt.% conductive carbon black was added during electrode preparation to minimize the polarization problem. The areal mass loading of the active material on each working electrode was 1 mg cm^{-2} unless specifically mentioned.

For the ASSC, PVA/H_2SO_4 gel was used as the electrolyte. The device was fabricated as follows: First, PVA (2 g) was added to DI water (15 ml) and heated to 80 °C under vigorous stirring until the solution became clear. Concentrated H_2SO_4 (2 g) in DI water (5 ml) was then added dropwise to the PVA solution and further stirred for 30 min. The formed PVA/H_2SO_4 solution was cast onto the working electrode and then dried at room temperature for 12 h. Finally, two symmetric electrodes were assembled without an additional separator and tightly sealed with Kapton tape to construct the device.

4.4. Electrochemical characterization and analysis

All electrochemical measurements were carried out on an Autolab (Metrohm PGSTAT302N) electrochemical workstation at room temperature (25 °C). The EIS tests were performed at open circuit potential with a sinusoidal signal at a frequency range from 100 kHz to 10 mHz at an amplitude of 10 mV. The cyclic stability was evaluated after continuous cycles at a constant charge-discharge current density of 10 A g^{-1}.

For the three-electrode configuration, the as-prepared working electrode was directly measured with Ag/AgCl and platinum foil as the reference and counter electrode, respectively, in 1.0 M KOH aqueous electrolyte. The galvanostatic specific capacitance was derived from GCD curves according to: $C_{wt} = (I \times \Delta t)/(m \times \Delta V)$, where C_{wt} is the galvanostatic specific capacitance (F g^{-1}); I is the discharge current (A); m is the mass loading of active material (g); Δt is the discharge time (s) and ΔV is the operating voltage (V) after IR-drop correction (subtracted by the V_{drop}). The quantitative capacitance differentiation was carried out in CV curves using: $i(V) = k_1 v + k_2 v^{1/2}$, where $i(V)$ is the current density at a fixed potential; k_1 is the capacitive effect factor; k_2 is the diffusion process factor and v is scan rate (mV s^{-1}). Thus, $k_1 v$ and $k_2 v^{1/2}$ in the equation represent the capacitive and diffusion-controlled contribution, respectively [30].

For symmetric supercapacitors and ASSC, the galvanostatic and volumetric specific capacitance of the activate material were calculated from GCD curves using: $C_{wt} = 2(I \times \Delta t)/(m \times \Delta V)$ and $C_{vol} = C_{wt} \times \rho$, respectively, where C_{vol} is volumetric specific capacitance (F cm^{-3}) and ρ is the compaction density of active material on working electrode (g cm^{-3}). The galvanostatic and volumetric energy density of two electrodes in device were derived by: $E_{wt} = (C_{wt} \times \Delta V^2)/8$ and $E_{vol} = E_{wt} \times \rho$, respectively, where E_{wt} is galvanostatic energy density (Wh kg^{-1}) and E_{vol} is volumetric energy density (Wh L^{-1}). The corresponding galvanostatic and volumetric power density were obtained from: $P_{wt} = E_{wt}/\Delta t$ and $P_{vol} = P_{wt} \times \rho$, respectively, where P_{wt} is galvanostatic power density (W kg^{-1}) and P_{vol} is volumetric power density (W L^{-1}). The stack volumetric energy density and stack volumetric power density of the entire device were calculated by: $E_{vol\text{-}stack} = E_{vol} \times f$ and $P_{vol\text{-}stack} = P_{vol} \times f$, respectively, where $E_{vol\text{-}stack}$ is stack volumetric energy density (Wh L^{-1}), $P_{vol\text{-}stack}$ is stack volumetric energy density (W L^{-1}) and f is the volume fraction of active materials in the entire device stack, which includes two active material pieces (each ~90 μm for 10 mg cm^{-2} areal mass loading), two current collectors (aluminium foils, each ~20 μm) and one separator (Celgard membrane, ~30 μm).

Acknowledgment

This work was supported by the EPSRC (Grant nos. EP/L018330/1 and EP/K002252/1). J.G. would like to thank the University College London and China Scholarship Council for the joint UCL-CSC Ph.D. scholarships.

Declaration of interests

The authors declared no conflicts of interests.

Appendix A. Supplementary material

Supplementary data associated with this article can be found in the online version at doi:10.1016/j.ensm.2018.12.006.

References

[1] P. Simon, Y. Gogotsi, Materials for electrochemical capacitors, Nat. Mater. 7 (2008) 845–854.
[2] M.F. El-Kady, Y. Shao, R.B. Kaner, Graphene for batteries, supercapacitors and beyond, Nat. Rev. Mater. 1 (2016) 1–14.
[3] R.K. Paul, M. Ghazinejad, M. Penchev, J. Lin, M. Ozkan, C.S. Ozkan, Synthesis of a pillared graphene nanostructure: a counterpart of three-dimensional carbon architectures, Small 6 (2010) 2309–2313.
[4] P. Ratajczak, M.E. Suss, F. Kaasik, F. Béguin, Carbon electrodes for capacitive technologies, Energy Storage Mater. 16 (2019) 126–145.
[5] Y. Zhu, S. Murali, M.D. Stoller, K.J. Ganesh, W. Cai, P.J. Ferreira, A. Pirkle, R.M. Wallace, K.A. Cychosz, M. Thommes, D. Su, E.A. Stach, R.S. Ruoff, Carbon-based supercapacitors produced by activation of graphene, Science 332 (2011) 1537–1541.
[6] F. Zhang, T. Liu, M. Li, M. Yu, Y. Luo, Y. Tong, Y. Li, Multiscale pore network boosts capacitance of carbon electrodes for ultrafast charging, Nano Lett. 17 (2017) 3097–3104.
[7] Y. Bu, T. Sun, Y. Cai, L. Du, O. Zhuo, L. Yang, Q. Wu, X. Wang, Z. Hu, Compressing carbon nanocages by capillarity for optimizing porous structures toward ultrahigh-volumetric-performance supercapacitors, Adv. Mater. 29 (2017) 1700470.
[8] Z. Lei, J. Zhang, L.L. Zhang, N.A. Kumar, X.S. Zhao, Functionalization of chemically derived graphene for improving its electrocapacitive energy storage properties, Energy Environ. Sci. 9 (2016) 1891–1930.
[9] A.J. Amali, J.K. Sun, Q. Xu, From assembled metal-organic framework nanoparticles to hierarchically porous carbon for electrochemical energy storage, Chem. Commun. 50 (2014) 1519–1522.
[10] S. Gadipelli, V. Krungleviciute, Z.-X. Guo, T. Yildirim, Exceptional CO 2 capture in a hierarchically porous carbon with simultaneous high surface area and pore volume, Energy Environ. Sci. 7 (2014) 335–342.
[11] P. Pachfule, D. Shinde, M. Majumder, Q. Xu, Fabrication of carbon nanorods and graphene nanoribbons from a metal–organic framework, Nat. Chem. 8 (2016) 718–724.
[12] S. Gadipelli, Z.X. Guo, Tuning of ZIF-derived carbon with high activity, nitrogen functionality, and yield - a case for superior CO2 capture, ChemSusChem 8 (2015) 2123–2132.
[13] Y. Xu, K. Sheng, C. Li, G. Shi, Self-assembled graphene hydrogel via a one-step hydrothermal process, ACS Nano 4 (2010) 4324–4330.
[14] S. Pei, H.M. Cheng, The reduction of graphene oxide, Carbon 50 (2012) 3210–3228.
[15] S. Park, R.S. Ruoff, Chemical methods for the production of graphenes, Nat. Nanotechnol. 4 (2009) 217–224.
[16] D.C. Marcano, D.V. Kosynkin, J.M. Berlin, A. Sinitskii, Z. Sun, A. Slesarev, L.B. Alemany, W. Lu, J.M. Tour, Improved synthesis of graphene oxide, ACS Nano 4 (2010) 4806–4814.
[17] K. Hu, X. Xie, T. Szkopek, M. Cerruti, Understanding hydrothermally reduced graphene oxide hydrogels: from reaction products to hydrogel properties, Chem. Mater. 28 (2016) 1756–1768.
[18] Y. Xu, Z. Lin, X. Zhong, X. Huang, N.O. Weiss, Y. Huang, X. Duan, Holey graphene frameworks for highly efficient capacitive energy storage, Nat. Commun. 5 (2014) 4554.
[19] Y. Tao, X. Xie, W. Lv, D.M. Tang, D. Kong, Z. Huang, H. Nishihara, T. Ishii, B. Li, D. Golberg, F. Kang, T. Kyotani, Q.H. Yang, Towards ultrahigh volumetric capacitance: graphene derived highly dense but porous carbons for supercapacitors, Sci. Rep. 3 (2013) 2975.
[20] B. Jiang, C. Tian, L. Wang, L. Sun, C. Chen, X. Nong, Y. Qiao, H. Fu, Highly concentrated, stable nitrogen-doped graphene for supercapacitors: simultaneous doping and reduction, Appl. Surf. Sci. 258 (2012) 3438–3443.
[21] Z.S. Wu, Y. Sun, Y.Z. Tan, S. Yang, X. Feng, K. Müllen, Three-dimensional graphene-based macro- and mesoporous frameworks for high-performance electrochemical capacitive energy storage, J. Am. Chem. Soc. 134 (2012) 19532–19535.
[22] J. Liu, W. Lv, W. Wei, C. Zhang, Z. Li, B. Li, F. Kang, Q.-H. Yang, A three-dimensional graphene skeleton as a fast electron and ion transport network for electrochemical applications, J. Mater. Chem. A 2 (2014) 3031.
[23] Y. Xu, C.Y. Chen, Z. Zhao, Z. Lin, C. Lee, X. Xu, C. Wang, Y. Huang, M.I. Shakir, X. Duan, Solution processable holey graphene oxide and its derived macrostructures for high-performance supercapacitors, Nano Lett. 15 (2015) 4605–4610.
[24] Y. Gogotsi, P. Simon, True performance metrics in electrochemical energy storage, Science 334 (2011) 917–918.
[25] H.C. Schniepp, J.L. Li, M.J. McAllister, H. Sai, M. Herrera-Alonson, D.H. Adamson, R.K. Prud'homme, R. Car, D.A. Seville, I.A. Aksay, Functionalized single graphene sheets derived from splitting graphite oxide, J. Phys. Chem. B 110 (2006) 8535–8539.
[26] Z. Li, S. Gadipelli, Y. Yang, Z. Guo, Design of 3D graphene-oxide spheres and their derived hierarchical porous structures for high performance supercapacitors, Small 13 (2017) 1702474.
[27] K.N. Kudin, B. Ozbas, H.C. Schniepp, R.K. Prud'homme, I.A. Aksay, R. Car, Raman spectra of graphite oxide and functionalized graphene sheets, Nano Lett. 8 (2008) 36–41.
[28] R. Raccichini, A. Varzi, S. Passerini, B. Scrosati, The role of graphene for electrochemical energy storage, Nat. Mater. 14 (2015) 271–279.
[29] K.S.W. Sing, D.H. Everett, R.A.W. Haul, L. Moscou, R.A. Pierotti, J. Rouquero, T. Siemieniewska, Reporting physisorption data for gas/solid systems with special reference to the determination of surface area and porosity (Recommendations 1984), Pure Appl. Chem. 57 (1985) 603–619.
[30] V. Augustyn, P. Simon, B. Dunn, Pseudocapacitive oxide materials for high-rate electrochemical energy storage, Energy Environ. Sci. 7 (2014) 1597–1614.
[31] P.L. Taberna, P. Simon, J.F. Fauvarque, Electrochemical characteristics and impedance spectroscopy studies of carbon-carbon supercapacitors, J. Electrochem. Soc. 150 (2003) A292–A300.
[32] M.F. El-Kady, V. Strong, S. Dubin, R.B. Kaner, Laser scribing of high-performance and flexible graphene-based electrochemical capacitors, Science 335 (2012) 1326–1330.
[33] S. Ardizzone, G. Fregonara, S. Trasatti, "Inner" and "outer" active surface of RuO2 electrodes, Electrochim. Acta. 35 (1990) 263–267.
[34] J. Luo, H.D. Jang, J. Huang, Effect of sheet morphology on the scalability of graphene-based ultracapacitors, ACS Nano 7 (2013) 1464–1471.
[35] S.H. Park, H.K. Kim, S.B. Yoon, C.W. Lee, D. Ahn, S.I. Lee, K.C. Roh, K.B. Kim, Spray-assisted deep-frying process for the in situ spherical assembly of graphene for energy-storage devices, Chem. Mater. 27 (2015) 457–465.
[36] X. Zhang, Z. Sui, B. Xu, S. Yue, Y. Luo, W. Zhan, B. Liu, Mechanically strong and highly conductive graphene aerogel and its use as electrodes for electrochemical power sources, J. Mater. Chem. 21 (2011) 6494–6497.
[37] Y. Zhu, S. Murali, M.D. Stoller, A. Velamakanni, R.D. Piner, R.S. Ruoff, Microwave assisted exfoliation and reduction of graphite oxide for ultracapacitors, Carbon 48 (2010) 2118–2122.
[38] J. Luo, J. Kim, J. Huang, Material processing of chemically modified graphene: some challenges and solutions, Acc. Chem. Res. 46 (2013) 2225–2234.
[39] M. Sevilla, G.A. Ferrero, A.B. Fuertes, Graphene-cellulose tissue composites for high power supercapacitors, Energy Storage Mater. 5 (2016) 33–42.
[40] C. Zhong, Y. Deng, W. Hu, J. Qiao, L. Zhang, J. Zhang, A review of electrolyte materials and compositions for electrochemical supercapacitors, Chem. Soc. Rev. 44 (2015) 7484–7539.
[41] E. Raymundo-Piñero, K. Kierzek, J. Machnikowski, F. Béguin, Relationship between the nanoporous texture of activated carbons and their capacitance properties in different electrolytes, Carbon 44 (2006) 2498–2507.
[42] H. Banda, B. Daffos, S. Périé, Y. Chenavier, L. Dubois, D. Aradilla, S. Pouget, P. Simon, O. Crosnier, P.-L. Taberna, F. Duclairoir, Ion sieving effects in chemically tuned pillared graphene materials for electrochemical capacitors, Chem. Mater. 30 (2018) 3040–3047.
[43] X. Yang, C. Cheng, Y. Wang, L. Qiu, D. Li, Liquid-mediated dense integration of graphene materials for compact capacitive energy storage, Science 341 (2013) 534–537.
[44] H. Li, Y. Tao, X. Zheng, J. Luo, F. Kang, H.-M. Cheng, Q.-H. Yang, Ultra-thick graphene bulk supercapacitor electrodes for compact energy storage, Energy Environ. Sci. 9 (2016) 3135–3142.
[45] Z. Chen, J. Wen, C. Yan, L. Rice, H. Sohn, M. Shen, M. Cai, B. Dunn, Y. Lu, High-performance supercapacitors based on hierarchically porous graphite particles, Adv. Energy Mater. 1 (2011) 551–556.
[46] D. Yu, K. Goh, H. Wang, L. Wei, W. Jiang, Q. Zhang, L. Dai, Y. Chen, Scalable synthesis of hierarchically structured carbon nanotube–graphene fibres for capacitive energy storage, Nat. Nanotechnol. 9 (2014) 555–562.
[47] F. Meng, Y. Ding, Sub-micrometer-thick all-solid-state supercapacitors with high power and energy densities, Adv. Mater. 23 (2011) 4098–4102.
[48] C. Liu, Z. Yu, D. Neff, A. Zhamu, B.Z. Jang, Graphene-based supercapacitor with an ultrahigh energy density, Nano Lett. 10 (2010) 4863–4868.
[49] Y. Xu, Z. Lin, X. Huang, Y. Liu, Y. Huang, X. Duan, Flexible solid-state supercapacitors based on three-dimensional graphene hydrogel films, ACS Nano 7 (2013) 4042–4049.
[50] Z. Weng, Y. Su, D.W. Wang, F. Li, J. Du, H.M. Cheng, Graphene-cellulose paper flexible supercapacitors, Adv. Energy Mater. 1 (2011) 917–922.
[51] S. Gadipelli, Y. Lu, N.T. Skipper, T. Yildirim, Z. Guo, Design of hyperporous graphene networks and their application in solid-amine based carbon capture systems, J. Mater. Chem. A 5 (2017) 17833–17840.
[52] S. Gadipelli, J. Burress, T. Yildrim, Graphene oxide derived carbons (GODCs): synthesis and gas adsorption properties, Energy Environ. Sci. 5 (2012) 6453–6459.